Supplementary Data

Supplementary Table S1. The IC Number for Each Network Is Shown Alongside the Visual Classification (with a Citation if Applicable), a Check Mark if the Network Was Included in Data Analysis and the Size of Each Network in Voxels

IC#	*Classification as network*	*Included*	*Size ($\times 10^4$ voxels)*
1	Thermal noise		1.77
2	Caudal default mode (Fox et al., 2005)	✓	2.04
3	White matter		2.23
4	Dorsal frontal cortex	✓	3.79
5	Parietal cortex	✓	2.30
6	White matter-CSF boundary		1.65
7	Insular cortex	✓	1.51
8	Primary visual (van de Heuven et al., 2010)	✓	1.15
9	Right frontoparietal (van de Heuven et al., 2010)	✓	2.43
10	Bilateral frontoparietal (van de Heuven et al., 2010)	✓	2.38
11	Ventral somatomotor cortex	✓	2.42
12	Extra-striate visual (van de Heuven et al., 2010)	✓	1.96
13	Left frontoparietal (van de Heuven et al., 2010)	✓	3.49
14	Entire somatomotor cortex	✓	2.60
15	Ventral frontal cortex	✓	4.26
16	Dorsal somatomotor cortex	✓	4.09
17	Task positive (Fox et al., 2005)	✓	2.00
18	Posterior cingulate cortex	✓	1.33
19	Entire default mode (Fox et al., 2005)	✓	2.65
20	CSF		3.32

CSF, cerebrospinal fluid.

SUPPLEMENTARY TABLE S2. BRODMANN REGIONS FROM WHICH AVERAGE CMR_{glc}, Bq/mL and T1 MPRAGE CONTRAST WERE CALCULATED IN FIGURE 1

1	Primary Somatosensory Cortex
4	Primary Motor Cortex
5	Somatosensory Association Cortex
6	Premotor Cortex, Supplementary Motor Cortex
7	Somatosensory Association Cortex, Precuneus
8	Includes Frontal Eye Field
9	Dorsolateral Prefrontal Cortex
10	Anterior Prefrontal Cortex
11	Orbitofrontal Area
13	Insular Cortex
17	Primary Visual Cortex (V1)
18	Secondary Visual Cortex (V2)
19	Associative Visual Cortex (V3)
20	Inferior Temporal Gyrus
21	Middle Temporal Gyrus
22	Superior Temporal Gyrus (caudal part is the Wernicke area)
23	Ventral Posterior Cingulate Cortex
24	Ventral Anterior Cingulate Cortex
25	Subgenual Cortex
30	Part of Cingulate Cortex
31	Dorsal Posterior Cingulate Cortex
32	Dorsal Anterior Cingulate Cortex
34	Anterior Entorhinal Cortex (on the parahippocampal gyrus)
36	Parahippocampal Cortex (on the parahippocampal gyrus)
37	Fusiform Gyrus
38	Temporopolar Area
39	Angular Gyrus, (part of Wernicke area)
40	Supramarginal Gyrus (part of Wernicke area)
41	Primary and Auditory Association Cortex
44	Pars Opercularis, part of Broca area
45	Pars Triangularis Broca area
46	Dorsolateral Prefrontal Cortex
47	Inferior Prefrontal Gyrus
48	Caudate
49	Putamen
50	Thalamus
51	Globus Pallidus
52	Nucleus Accumbens
53	Amygdala
54	Hippocampus
55	Hypothalamus

CMR_{glc}, cerebral metabolic rate of glucose consumption.

Supplementary Table S3. Linear Regression Results for Scatter Plots Shown in Supplementary Figures 7 and 8

Supplementary figures	*X-axis*	*Y-axis*	*Nuisance signal regression?*	R^2	*Slope*	*Slope,* p	*Inter-cept*	*Inter-cept,* p
7A	CMR_{glc}, eyes closed	CMR_{glc}, eyes open	N/A	0.907	1.11	0	−0.0002	0.501
7B	Variance, eyes closed	Variance, eyes open	No	0.315	0.818	0	11.3	0
7C	ALFF, eyes closed	ALFF, eyes open	No	0.714	1.03	0	0.0356	0
7D	FALFF, eyes closed	FALFF, eyes open	No	0.514	0.846	0	0.0189	0
7E	Short-range FCD, eyes closed	Short-range FCD, eyes open	No	0.712	1.04	0	0.304	0
7F	Long-range FCD, eyes closed	Long-range FCD, eyes open	No	0.334	0.715	0	33.7	0
7G	Short-range FCD, eyes closed	Short-range FCD, eyes open	Yes	0.606	0.812	0	0.25	0
7H	Long-range FCD, eyes closed	Long-range FCD, eyes open	Yes	0.137	0.319	0	2.63	0
7I	Whole-brain correlation, eyes closed	Whole-brain correlation, eyes open	N/A	0.547	0.905	0	1.1	0
8A	Short-range FCD	CMR_{glc}	No	0.185	0.0166	0	0.283	0
8B	Short-range FCD	Whole-brain correlation	No	0.694	0.894	0	2.06	0
8C	CMR_{glc}	Whole-brain correlation	N/A	0.179	11.5	0	0.433	0
8D	FALFF	CMR_{glc}	No	0.172	0.0437	0	0.313	0
8E	Short-range FCD	FALFF	No	0.683	0.302	0	−0.527	0
8F	FALFF	Whole-brain correlation	No	0.695	2.39	0	3.74	0

Columns show equivalent scatter plot, what is plotted on *X* and *Y* axes, whether nuisance signal regression was done, R^2 for linear fit and values for slope, *p* value from *T*-test for slope, *Y*-intercept, and *p* value from *T*-test for *Y*-intercept. (Very low *p* values less than 2.22×10^{-16} resolved to zero.) *T*-tests were done using ''regstats.m'' function in *MATLAB*. Only gray matter voxels were used for statistics here. All slopes and intercepts are significant with the exception of the *Y*-intercept for CMR_{glc} with eyes closed versus eyes open. Results that showed a global increase in the eyes open condition show either a >1 slope or a >0 intercept, or both, for example, Supplementary Figure S7A, E and I. All different metrics showed a strong linear relationship with each other in terms of topology; this has been shown previously by Aiello et al. (2015) See their work for further analysis, including better consideration of shared topological variation due to anatomy, etc.

ALFF, amplitude of low-frequency fluctuation; FALFF, fractional ALFF.

Supplementary Table S4. Tests of Differing Types of Nuisance Signal Regression

			Mean signals			*Motion parameters*					
	No.	*Tested*	*Whole-brain*	*White matter*	*CSF*	*Right*	*Fwd.*	*Up*	*Pitch*	*Roll*	*Yaw*
Main study	i	All									
	ii	All	X	X	X	X	X	X	X	X	X
Supplementary Data	iii	Short-range FCD		X	X	X	X	X	X	X	X
	iv	Short-range FCD		X		X	X	X	X	X	X
	v	Short-range FCD			X	X	X	X	X	X	X
	vi	Short-range FCD				X	X	X	X	X	X

The columns are, from left to right: whether the test was done in the main study or the Supplementary Data, the Roman numeral designator, which R-fMRI metrics were tested with these regressions, and then the rest of the columns have an ''X'' if the signal listed at the top of the column was included in this set of regressions, or blank if it was not. (i) and (vi) produced similar results, and (ii), (iii), (iv), and (v) produced similar results. fMRI, resting state functional magnetic resonance imaging.

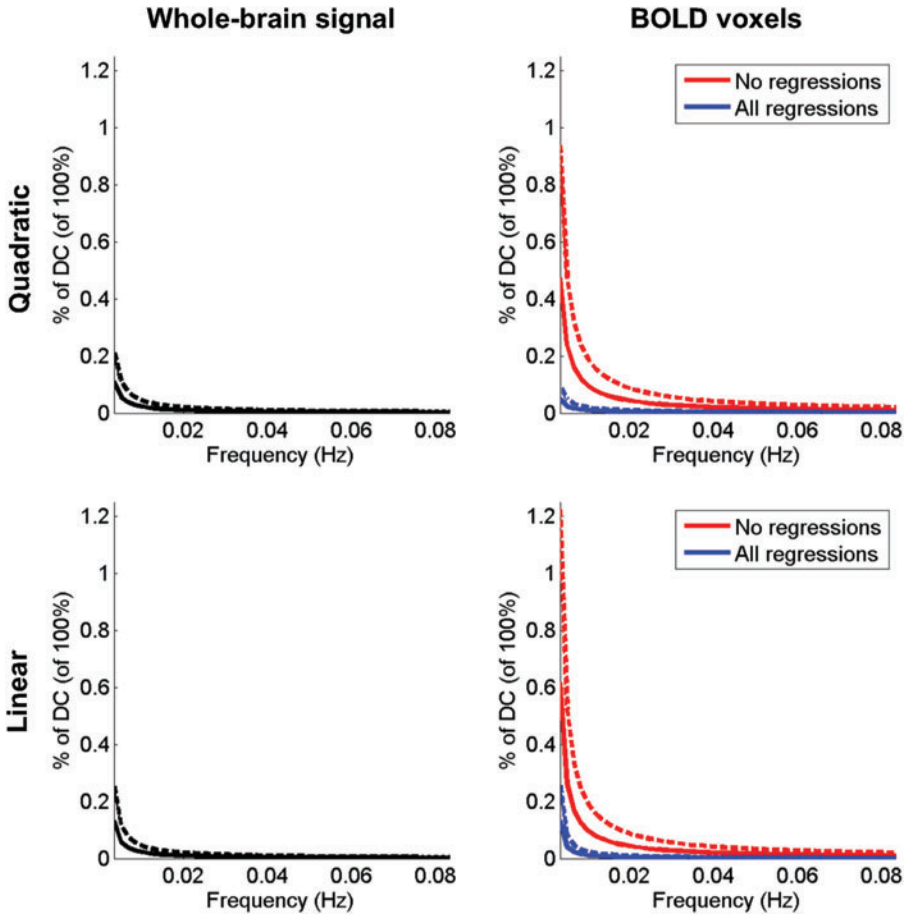

SUPPLEMENTARY FIG. S1. Frequencies affected by quadratic detrend (used in this study) and linear detrend (also commonly used). *X*-axis is frequency, *Y*-axis is amplitude expressed as percentage of DC amplitude. (i.e., divide each amplitude by the amplitude at the zero frequency times 100%, producing a value from 0% to 100%. In the plots, the *X*-axis has a minimum value of 0.0017 Hz shown.) Solid lines are means; dashed lines are mean+one standard deviation. Left column is the FFT of the trend removed from the whole-brain signal, right column is the FFT of the trend removed from individual voxels (mean is across all subjects and all voxels). Top row is a quadratic trend; bottom row is a linear trend. Red lines are voxels without any regressions; blue lines are voxels with all regressions (not applicable to global signal, as it is a regressor itself). There is little difference between quadratic and linear detrends except at the lowest (<0.005 Hz) frequencies where linear has a slightly larger effect. There is a lesser effect of detrending on the global signal itself, or if all regressions are done on voxels, versus the voxels' original signals with no regressions done. All effects are visibly similar to negative exponential functions. FFT, fast Fourier transformation.

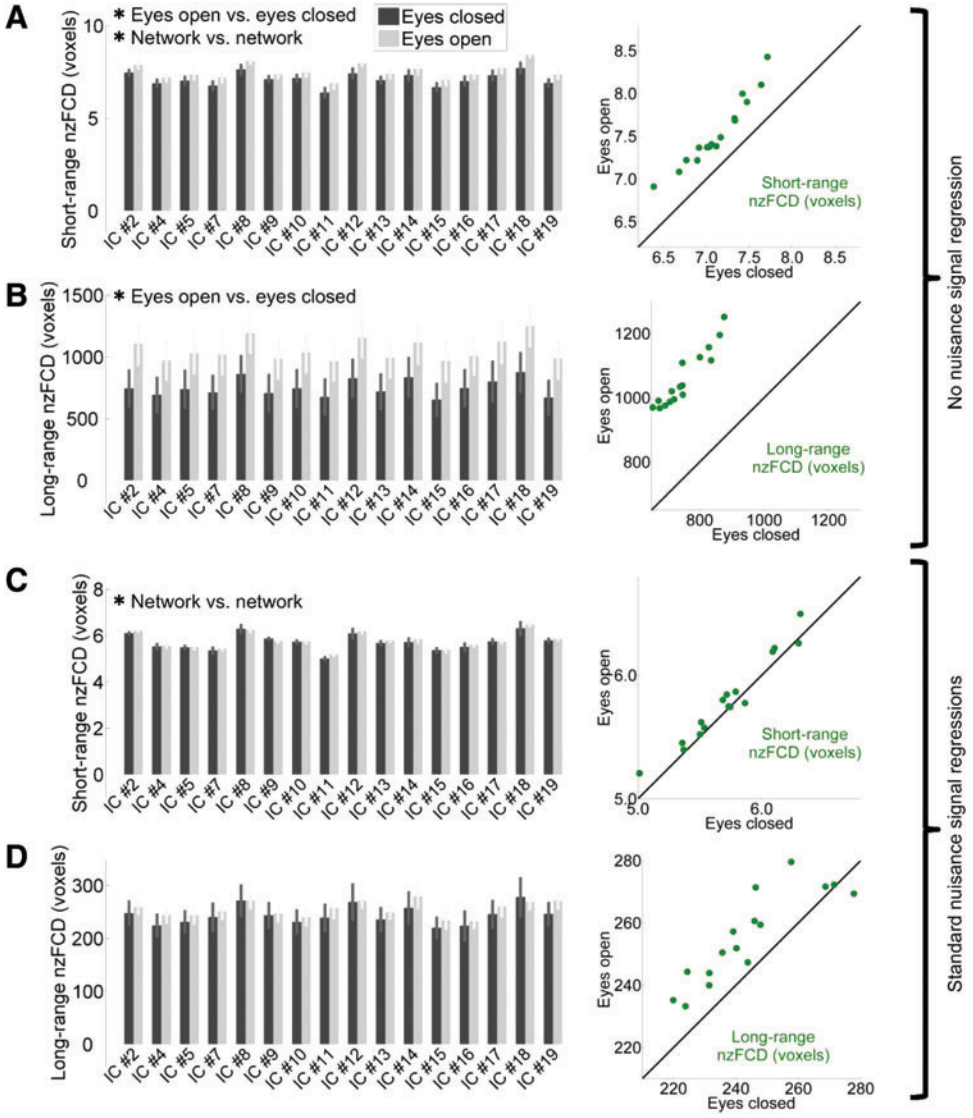

SUPPLEMENTARY FIG. S2. Post-hoc test. Reducing the threshold for connections from $r = 0.6$ to $r = 0.25$ for FCD-based metrics increases statistical significance but does not change overall trends. Left: The mean in each network is shown on the *Y*-axis with numbered networks along the *X*-axis. Error bars are one standard error. Dark gray is $N = 11$ in the eyes closed condition, light gray is $N = 11$ in the eyes open condition. Right: Scatter plot with each network as a point, mean of each metric ($N = 11$) in the eyes closed condition as the *X*-axis, mean of each metric ($N = 11$) in the eyes open condition as the *Y*-axis. Results without nuisance signal regression are shown for A and B, results with full nuisance signal regression are shown for C and D. Black line is $Y = X$. All values are number of connected voxels. Significance threshold is from the main text ($p \leq 8.9 \times 10^{-4}$). **(A)** Short-range nzFCD with threshold 0.25, like threshold 0.6, is significantly greater in the eyes open condition (*), but unlike threshold 0.6 is also significantly different network to network (*). ($p = 5.66 \times 10^{-5}$ for network vs. network, $p = 7.57 \times 10^{-5}$ for eyes open vs. eyes closed, $p = 1.00$ for interaction.) **(B)** Long-range nzFCD with threshold 0.25 is, unlike threshold 0.6, significantly greater in the eyes open condition (*) but remains nonsignificantly different network to network. ($p = 0.962$ for network vs. network, $p = 2.28 \times 10^{-7}$ for eyes open vs. eyes closed, $p = 1.00$ for interaction.) **(C)** As **(A)**, but with full nuisance signal regression. Eyes closed versus eyes open is no longer significant, though network versus network remains significant. ($p = 5.18 \times 10^{-18}$ for network vs. network, $p = 0.236$ for eyes open vs. eyes closed, $p = 1.00$ for interaction.) **(D)** As **(B)**, but with full nuisance signal regression. Eyes closed versus eyes open is no longer significant. ($p = 0.596$ for network vs. network, $p = 0.167$ for eyes open vs. eyes closed, $p = 1.00$ for interaction.) These results are very similar to the greater threshold, as shown in Figures 3B and 4B and Supplementary Figure S3, except that *p* values are lower and there is more significance.

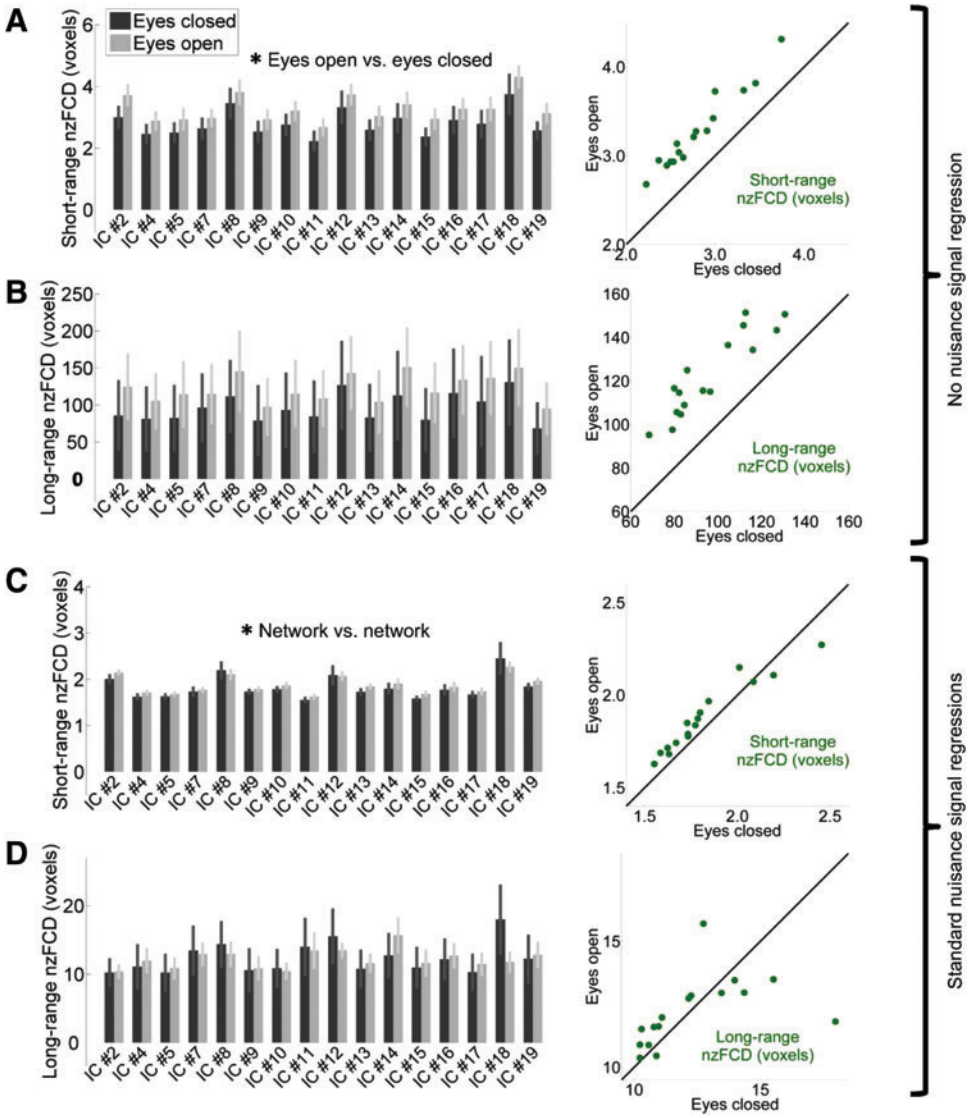

SUPPLEMENTARY FIG. S3. Result from main text. FCD-based metrics with standard $r = 0.6$ threshold. Left: The mean in each network is shown on the *Y*-axis with numbered networks along the *X*-axis. Error bars are one standard error. Dark gray is $N = 11$ in the eyes closed condition, light gray is $N = 11$ in the eyes open condition. Right: Scatter plot with each network as a point, mean of each metric ($N = 11$) in the eyes closed condition as the *X*-axis, mean of each metric ($N = 11$) in the eyes open condition as the *Y*-axis. Results without nuisance signal regression are shown. Black line is $Y = X$. All values are number of connected voxels. **(A and B)** FCD-based metrics have similar behavior to FDG. **(A)** Short-range nzFCD which, like FDG, is significantly greater in the eyes open condition (*) but not significantly different network to network. **(B)** Long-range nzFCD, which has the same trend as short-range nzFCD but is not significant. FCD with zeros included in averaging was very similar to nzFCD except with less statistical significance. Total nzFCD (not shown) was very similar to long-range nzFCD. Voxel-wise scatter plots are shown in Supplementary Figure S7E, F. **(C–D)** Nuisance signal regression eliminates the state difference in FCD. **(C)** Identical to **(A)**, except nuisance signal regression was performed before calculating FCD. **(D)** Identical to **(B)**, except nuisance signal regression was performed before calculating FCD. The previous observation, that the mean result for eyes open was always larger than the mean result for eyes closed, has been lost. Instead, short-range nzFCD is now significantly different network to network (*). Voxel-wise scatter plots are shown in Supplementary Figure S7G, H. Statistics are given in Table 1. FCD, functional connectivity density; FDG, fluoro-deoxyglucose; nzFCD, FCD with zeros removed for averaging purposes only.

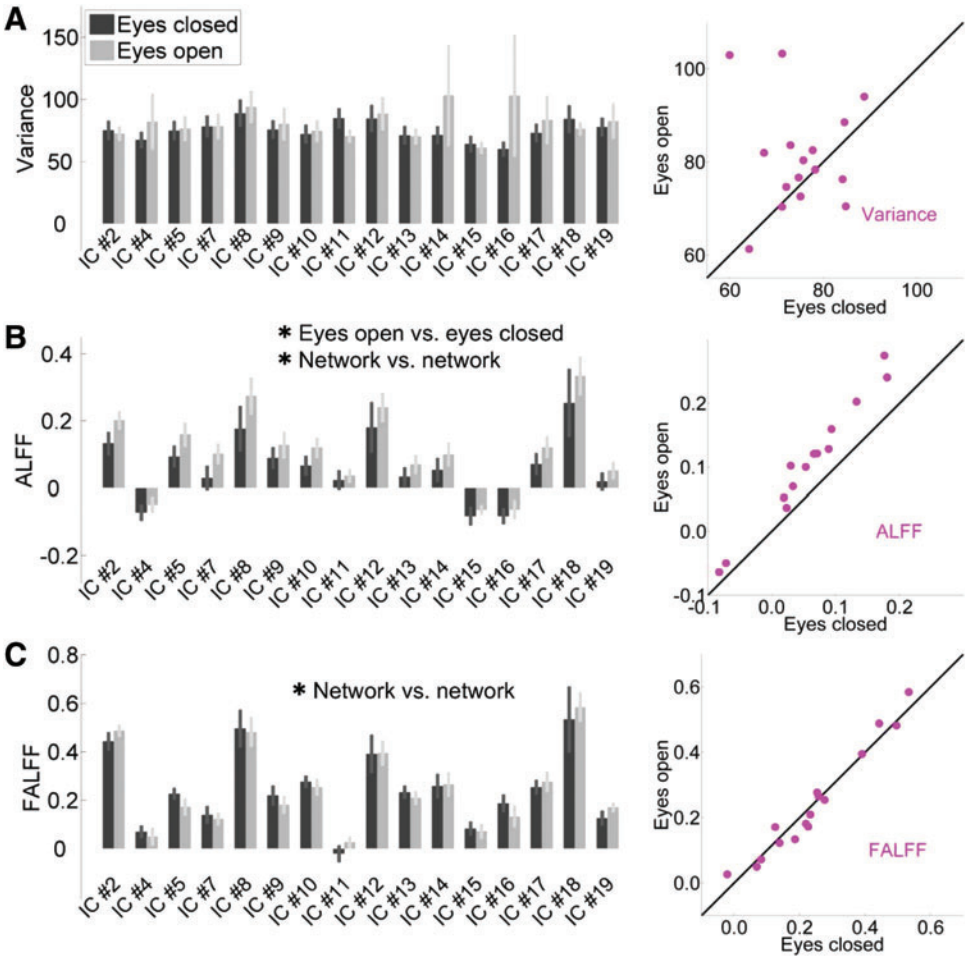

SUPPLEMENTARY FIG. S4. Result from main text. Variance-based metrics do not well approximate FDG. Left: The mean in each network is shown on the *Y*-axis with numbered networks along the *X*-axis. Error bars are one standard error. Dark gray is $N=11$ in the eyes closed condition, light gray is $N=11$ in the eyes open condition. Right: Scatter plot with each network as a point, mean of each metric ($N=11$) in the eyes closed condition as the *X*-axis, mean of each metric ($N=11$) in the eyes open condition as the *Y*-axis. Black line is $Y=X$. Results without nuisance signal regression are shown. **(A)** Broadband variance, which differs insignificantly network versus network or condition versus condition. **(B)** ALFF, which varies significantly network versus network and condition versus condition (*). **(C)** FALFF, which varies significantly network versus network (*) but not condition versus condition. Results with nuisance signal regression are very similar with identical significance except that ALFF is no longer significant for condition versus condition. Voxel-wise scatter plots are shown in Supplementary Figure S7B–D. Statistics are given in Table 1. ALFF, amplitude of low-frequency fluctuation; FALFF, fractional ALFF.

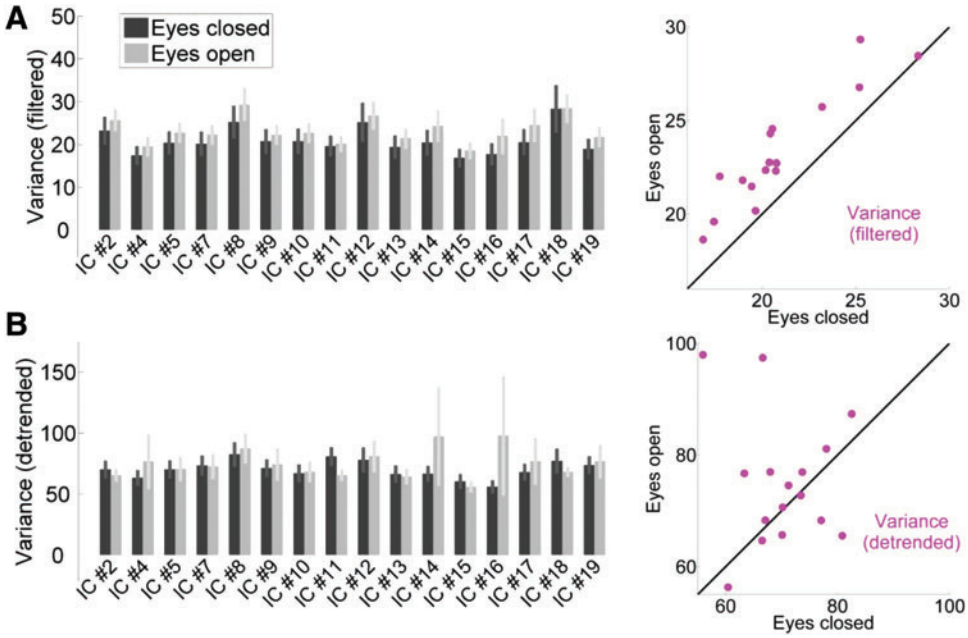

SUPPLEMENTARY FIG. S5. Post-hoc test. Broadband variance after alternate preprocessing also does not show significant eyes open versus eyes closed or network versus network differences. Left: The mean in each network is shown on the *Y*-axis with numbered networks along the *X*-axis. Error bars are one standard error. Dark gray is $N = 11$ in the eyes closed condition, light gray is $N = 11$ in the eyes open condition. Right: Scatter plot with each network as a point, mean of each metric ($N = 11$) in the eyes closed condition as the *X*-axis, mean of each metric ($N = 11$) in the eyes open condition as the *Y*-axis. Black line is $Y = X$. Results are without nuisance signal regression. **(A)** Broadband variance except calculated after filtering using the same filter as was used for FCD (a hard-edged Fourier filter with pass-band 0.01–0.08 Hz). It has low ($p < 0.05$) p values but is not significant (using the threshold from the main text, $p \leq 8.9 \times 10^{-4}$) for both network versus network and eyes open versus eyes closed ($p = 0.0229$ for network vs. network, $p = 0.0311$ for eyes open vs. eyes closed, $p = 1.00$ for interaction). Other than having a higher mean, the network to network height differences appear similar to ALFF shown in Supplementary Figure S4B. **(B)** Broadband variance except calculated after removing a quadratic trend from the data. It is nonsignificant for both network versus network and condition versus condition ($p = 0.983$ for network vs. network, $p = 0.364$ for eyes open vs. eyes closed, $p = 0.959$ for interaction). This result is almost identical to not having performed the detrending, as shown in Supplementary Figure S4A.

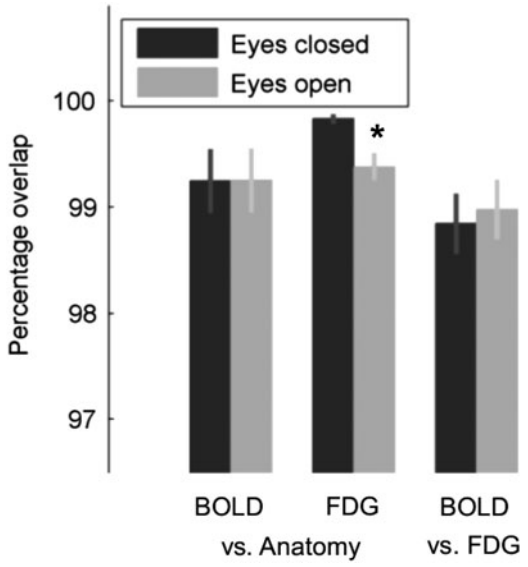

SUPPLEMENTARY FIG. S6. Overlap of whole-brain masks for different modalities. Mean ± one standard error is shown, eyes closed as dark gray, eyes open as light gray. Whole-brain masks were generated with SPM8 for co-registered BOLD, FDG, and anatomical MRI (''Anatomy'') and were compared in terms of percentage overlap. All overlap is very high ($\sim$98–100%). There is a small (0.45%) but significant (*, $p = 0.0036$) difference between eyes closed and eyes open subjects' registrations only for FDG versus anatomical MRI. ($N = 11$ per group, modality.)

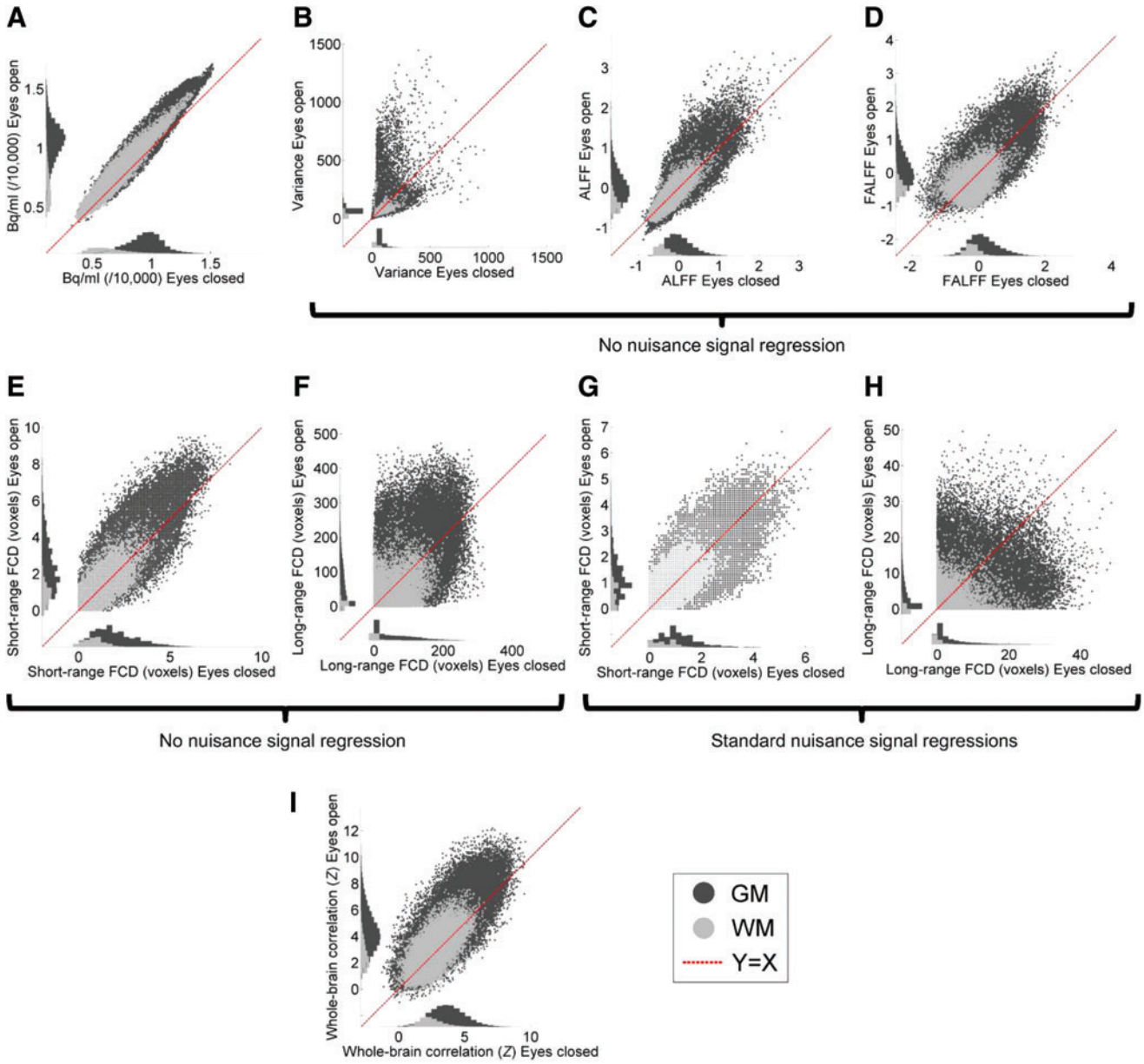

SUPPLEMENTARY FIG. S7. Within-metric, between-state scatter plots for all voxels in gray matter and white matter, excluding the cerebellum. All subjects within a group (eyes open or eyes closed) were averaged together for a given metric, and the voxel's value for that metric in the eyes closed condition plotted on the *X*-axis and the same voxel's value for that metric in the eyes open condition plotted on the *Y*-axis. Gray matter voxels are shown as dark gray dots, white matter voxels are shown as light gray dots. The red dashed line is the identity line of $X = Y$ in every case. Histograms are shown for gray matter and white matter along each axis, 40 bins, scaled in the axis direction to match the scatter plot, scaled in the other direction arbitrarily for display purposes. Unless otherwise noted, nuisance signal regression was not performed. **(A)** FDG as shown in the main text, Figure 3A. **(B)** Broadband variance as shown in Supplementary Figure S4A. **(C)** ALFF as shown in Supplementary Figure S4B. **(D)** FALFF as shown in the main text, Figure 3D. **(E)** Short-range FCD as shown in the main text, Figure 3B. **(F)** Long-range FCD as shown in Supplementary Figure S3B. **(G)** Short-range FCD with nuisance signal regression as shown in Supplementary Figure S3C. Color is lighter as this metric falls into fewer discrete values, thus the white background is not completely occluded by dots. **(H)** Long-range FCD with nuisance signal regression as shown in Supplementary Figure S3D. **(I)** Correlation (*Z*) with the whole-brain signal as shown in the main text, Figure 3C. Note that, while data are noisy, all of the trends seen in the main text as an increase from baseline can be seen here as either an increased slope or an upward shift from the identity line. Statistics for line fits on gray matter voxels are shown in Supplementary Table 3.

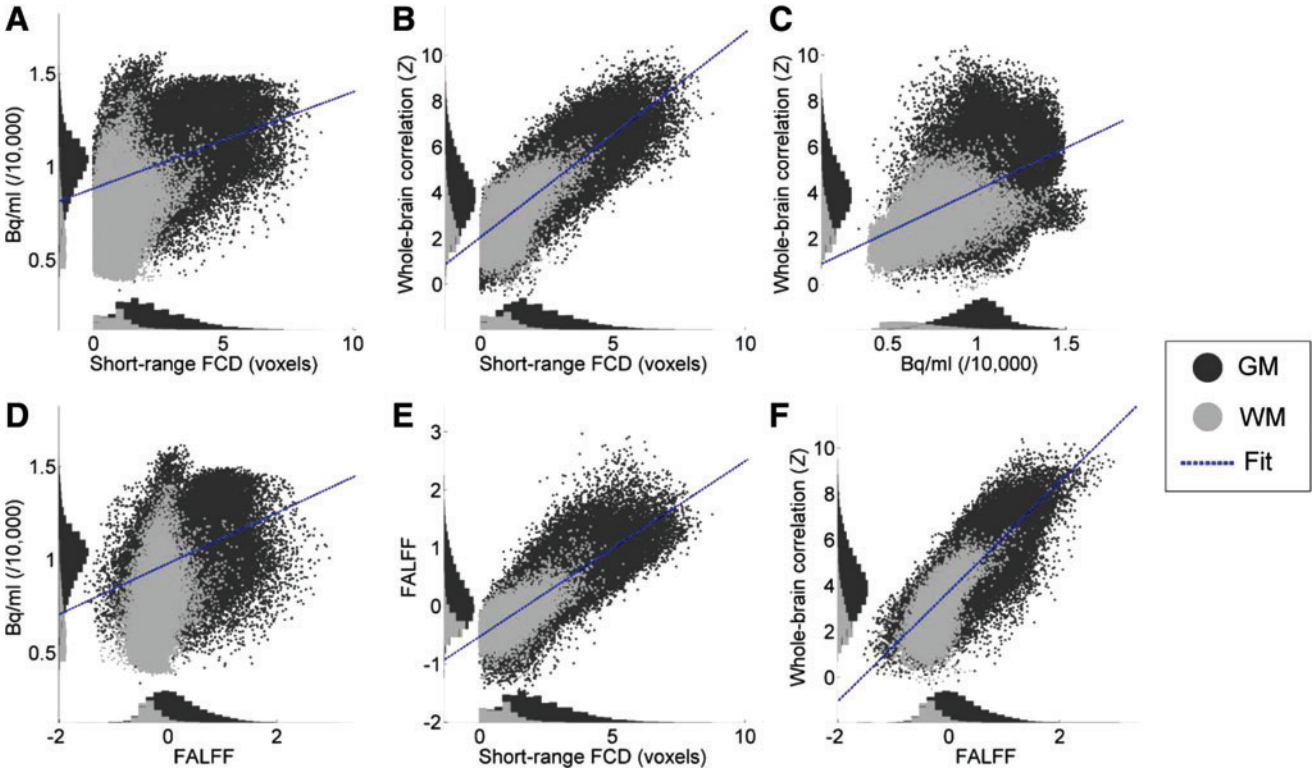

SUPPLEMENTARY FIG. S8. Between-metric scatter plots for all voxels in gray matter and white matter, excluding the cerebellum. Eyes open and eyes closed groups were combined for this figure. All subjects were averaged together for a given metric, and the voxel's value for one metric plotted on the *X*-axis and the same voxel for another metric plotted on the *Y*-axis. Gray matter voxels are shown as dark gray dots, white matter voxels are shown as light gray dots. The blue dashed line is a least-squares linear fit between the two metrics using gray matter voxels only. Histograms are shown for gray matter and white matter along each axis, 40 bins, scaled in the axis direction to match the scatter plot, scaled in the other direction arbitrarily for display purposes. Nuisance signal regression was not performed on any of the metrics shown. **(A)** Short-range FCD on the *X*-axis, FDG on the *Y*-axis. **(B)** Short-range FCD on the *X*-axis, whole-brain correlation on the *Y*-axis. **(C)** FDG on the *X*-axis, whole-brain correlation on the *Y*-axis. **(D)** FALFF on the *X*-axis, FDG on the *Y*-axis. **(E)** Short-range FCD on the *X*-axis, FALFF on the *Y*-axis. **(F)** FALFF on the *X*-axis, whole-brain correlation on the *Y*-axis. Compare results to Aiello et al. (2015), Figures 2 and 3. Statistics for line fits on gray matter voxels are shown in Supplementary Table S3.

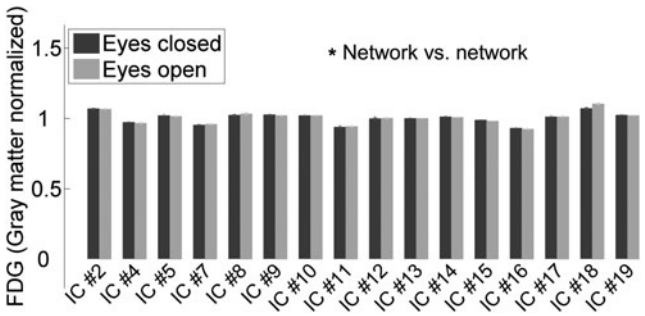

SUPPLEMENTARY FIG. S9. FDG result after performing gray matter normalization. As Figure 3A, except each voxel's value was divided by the mean value from all gray matter voxels. This eliminates any significant eyes open versus eyes closed difference and creates a significant network versus network difference.

Section S1: Details of Image Registration Method

Statistical Parametric Mapping (SPM8, www.fil.ion.ucl.ac.uk/spm/software/spm8) and BioImage Suite (bioimagesuite.yale.edu) were used through MATLAB version 2014A (www.mathworks.com) along with custom MATLAB functions to perform all preprocessing steps, including resting state functional magnetic resonance imaging (R-fMRI) preprocessing functions originally created by Majeed et al. (2011).

Slice timing correction (R-fMRI), motion correction (R-fMRI), and segmentation (mean R-fMRI, positron emission tomography [PET], and anatomical MRI) were conducted in SPM8 in that order, with default parameters except that the middle (150th) volume was used as the reference for motion correction. The Brain Extraction Tool (fsl.fmrib.ox.ac.uk/fsl/fslwiki/BET) was used to create a per-subject ''whole-brain mask'' (mean R-fMRI).

Cross-modality image registration and normalization to the Montreal Neurological Institute (MNI) template brain were conducted in BioImage Suite on a per subject basis. The gray and white matter, 2 mm isotropic voxels, MNI standard template from BioImage Suite was used. All registrations used default parameters except for 50 iterations, cross-correlation used as the distance metric, and as specified below. Due to contrast differences across all three modalities (PET, R-fMRI, and anatomical MRI), the gray and white matter probability maps (created from segmentation in SPM8) were used for registration and normalization rather than the original images. The MNI template had values of 1.0 in all white matter and 0.5 in all gray matter. Thus, to create matching contrast for registration purposes, each gray matter probability map from anatomical MRI was multiplied by 0.5 (so 100% probability of gray matter equaled 0.5) and added to the equivalent white matter probability map (so 100% probability of white matter equaled 1.0) on a per-subject basis. This produced, in the original anatomical space, a map of similar contrast to the MNI template. A nonlinear registration was performed from that image to the template brain, giving the transformation ''from anatomical to template space.'' The anatomical MRI's gray matter probability map was blurred with a Gaussian kernel ($\sigma = 7$ mm) and the gray matter probability map from the mean R-fMRI image was affine linearly registered to it, to give the transformation ''from R-fMRI space to anatomical space.'' The PET gray matter probability map was also affine linearly registered to the blurred anatomical MRI gray matter, to give the transformation ''from PET space to anatomical space.'' (For subjects 7 and 20 the affine linear transformations were calculated in the opposite direction and reversed due to an error occurring if the standard direction was used.)

Following calculation of all transformations, they were applied as follows. Each image in the R-fMRI data, mean R-fMRI image, probability maps from it, and whole-brain mask all had the transformations ''from R-fMRI space to anatomical space'' first and ''from anatomical space to template space'' second applied. The PET image and the probability maps from it all had the transformations ''from PET space to anatomical space'' first and ''from anatomical space to template space'' second applied. The anatomical MRI image and the probability maps from it all had the transformation ''from anatomical space applied to template space'' applied. The anatomical MRI images, mean R-fMRI images, and PET images were compared visually by a researcher for all subjects to the template image using the brain outline, lateral sulcus, and cerebellar-cerebral divide as landmarks. Visual inspection confirmed a tight registration to the template for all three modalities (PET, R-fMRI, and anatomical MRI) and all subjects. Additional tests of registration accuracy are described in Section S8.

SPM8 motion correction on each R-fMRI run provided six motion parameters: three translations (right, forward, and up) and three rotations (pitch, roll, and yaw). For each subject and motion parameter, the maximum deviation was taken by subtracting its minimum value from its maximum value over the entire time series.

Section S2: Network Generation

Networks were generated using Independent Component Analysis (ICA). ICA has been shown to produce consistent results across different subjects and over multiple runs (Chen et al., 2008; Damoiseaux et al., 2006; Franco et al., 2009; Margulies et al., 2010; Meindl et al., 2010; Zuo et al., 2010). This was conducted using the Group ICA of fMRI Toolbox (GIFT; mialab.mrn.org/software/gift/) (Correa et al., 2007). Before running GIFT each three-dimensional R-fMRI image in 2 mm MNI space was blurred with a Gaussian kernel with a full-width, half-maximum (FWHM) of 8 mm and a kernel size of 6 mm isotropic. ICA was run on all 22 subjects together. All default parameters in GIFT were used. This process produced 20 T maps, each from an independent component (IC #1–IC #20). Each T map was thresholded at $p \leq 0.05$ corrected for Type I errors using sequential goodness of fit (SGoF) (Carvajal-Rodriguez et al., 2009) to produce a network mask for each IC. Resultant network sizes are shown in Supplementary Table S1.

A template of brain regions for the 2 mm MNI brain (Holmes et al., 1998) was used to define voxels being located in gray matter, white matter, or cerebrospinal fluid (CSF), and in either the cerebrum or cerebellum. (The same template could be used for all subjects, as all subjects were in 2 mm MNI space at this point.) In every network, voxels outside of gray matter or white matter, and voxels in the cerebellum, were excluded from the network mask. This was conducted to focus on cerebral networks and also save computational time. The cerebellum was not fully imaged in some subjects and was excluded for this reason.

All 20 networks were plotted against a mean 2 mm MNI template brain and visually inspected. The networks were categorized according to either their cortical regions or similar appearance to previously published networks. These classifications are shown in Supplementary Table S1. To focus on cortical networks, four networks were excluded from further analysis. These networks included IC #1, corresponding to thermal noise, IC #3, corresponding to white matter, IC #6, corresponding to the white matter/CSF boundary, and IC #20, corresponding to CSF. Other than exclusion of noncortical networks, these classifications were for informational purposes only and all networks were treated equally during data analysis.

Section S3: Preprocessing of R-fMRI Metrics

All R-fMRI metrics were calculated in 2 mm MNI space to match cerebral metabolic rate of glucose consumption (CMR_{glc}) results and network masks.

Before calculation of R-fMRI metrics, all data were set to zero outside of the whole-brain mask and loaded into MATLAB for further processing. Each 3D R-fMRI image (in 2 mm MNI space, 300 per run) was separately blurred using a Gaussian kernel with a FWHM of 8 mm and an isotropic kernel size of 6 mm. Gray matter, CSF, and white matter masks were created by thresholding the respective anatomical MRI probability maps at $p > 0.8$.

For all types of R-fMRI analysis, two types of nuisance signal regression were conducted: (i) not running any nuisance signal regression at all, (ii) regressing nine signals from each voxel, which were the six motion parameters from motion correction (three translation, three rotation) and the mean R-fMRI signals of the whole-brain, white matter, and CSF masks. These two basic sets of regressions (none vs. all) were chosen for simplicity; ''no regressions'' was particularly important as even regression of minor motion variation could introduce artifactual shared variance into the signal, and ''all regressions'' was particularly important because this follows typical R-fMRI preprocessing. See Section S7 for alternative subsets of regressions.

Section S4: Time Considerations

Calculation of both ALFF and FALFF took less than 5 sec per R-fMRI run. Without down-sampling, each R-fMRI run would have taken over 24 h to calculate functional connectivity density (FCD), with down-sampling this was reduced to $\sim$1.25 h. Calculation of whole-brain correlation took less than 30 sec per subject. The computer used was a Dell Precision T7600 with Intel(R) Xeon(R) CPU E5-2687W 0 @ 3.10 GHz, 64 GB RAM, Windows 7 SP1 64-bit OS.

Section S5: FCD Preprocessing

FCD-based metrics were calculated from the R-fMRI signal. These metrics are degree-based, as they are based on the number of voxels that a given voxel is strongly correlated with, or ''connected to'' functionally (Tomasi and Volkow, 2010). Before calculation of FCD, each voxel's time series was filtered to between 0.01 and 0.08 Hz with a boxcar in the Fourier domain and set to zero mean, unit standard deviation. The number of correlations was calculated between each voxel and all voxels in a down-sampled brain to reduce computational time. Comparison between FCD maps resulting from down-sampled and nondown-sampled comparisons appeared quite similar, except the number of connections was scaled down based on extent of down-sampling. The amount that was chosen to down-sample was 4.5 voxels in each dimension (So skip four voxels, then five voxels, then four voxels, then five voxels, etc.). This level of down-sampling was chosen as it guaranteed a minimum of eight comparable voxels and a maximum of 27 comparable voxels (the median value was also 27 comparable voxels) within a cube of six (original) voxels in each direction (thus a $13 \times 13 \times 13$ cube). (Note that the actual calculation of FCD used a sphere, the cube was just used for estimation of loss due to down-sampling, see Section FCD-based R-fMRI metrics: short-range, long-range, and total FCD in Methods for the actual data analysis.) The differences in the number of comparable voxels occur over lines of only one voxel horizontally or vertically, ensuring that FCD differences resulting from down-sampling across any brain region larger than 2 mm (all brain regions tested herein) will average out.

FCD is calculated on a per-voxel basis by counting the number of above-threshold connections between that voxel and other voxels. As in the original FCD studies, Pearson correlation was used to calculate connections with $r > 0.60$ used to indicate a connection (Tomasi and Volkow, 2010, 2011). Unlike some of the original studies, FCD was not given an upper limit on the number of connections. After observation of the main results, additional post hoc tests with $r > 0.25$ were done also, for details see Section S6 below.

Two methods were used for averaging together FCD. First, all values in the network were averaged including zero values (referred to as FCD) as this was done in previous studies that calculated FCD in hubs (Tomasi and Volkow, 2011), second, only nonzero values in the network were averaged (referred to as nonzero FCD or nzFCD), as this may increase signal to noise ratio by only measuring reporting voxels. Note that, unlike when zeros are included, long-range nzFCD can be higher than total nzFCD because subtraction of short-range FCD from total FCD can set voxels to zero, thus removing low-valued voxels from averaging.

Section S6: Consideration of Type II Errors

While SGoF does reduce Type II (false negative) errors compared to older methods, any form of multiple comparisons correction increases the chance of Type II errors. Thus, likely candidates for such errors are discussed in this section.

FCD-based metrics

Due to the high standard error observed for long-range nzFCD, it is possible that a Type II statistical error (false negative) has been made in considering it nonsignificant. To reduce the standard error by increasing the number of connections, the threshold for counting voxels as linked was reduced from $r = 0.60$ to $r = 0.25$ in a post hoc test that used the same methods and significance threshold as the main study. While this is much lower than has been used for FCD (Tomasi and Volkow, 2010) it is similar to earlier work on degree of connectivity and hierarchical clustering of R-fMRI voxels (Buckner et al., 2009; Cordes et al., 2002). Results from this are shown in Supplementary Figure S2. To summarize, before nuisance signal regression short-range nzFCD with $r = 0.25$ threshold was significantly different network versus network and eyes open versus eyes closed, and long-range nzFCD with $r = 0.25$ threshold was significantly different eyes open versus eyes closed. Following nuisance signal regression, only short-range nzFCD with $r = 0.25$ threshold was only significant network versus network. This result suggests that the nonsignificance of short-range FCD for network versus network and long-range FCD for eyes open versus eyes closed may be Type II statistical errors.

Variance-based metrics

The fact that there were few changes due to regression indicates that broadband variance and FALFF do not reflect characteristics of the signals that were regressed, even though the internal normalization of FALFF is very different from

nuisance signal regression (Zou et al., 2008). Due to concerns that broadband variance may have been sensitive to very low or very high frequencies, thus eliminating significance, post hoc tests was done where variance was calculated either following a quadratic detrend (as linear detrend, except with quadratic equation, see Section S11 below and Supplementary Figure S1 for discussion of the frequencies affected), or following band-pass filtering to the 0.01 to 0.08 Hz band. These results are shown in Supplementary Figure S5. To summarize, no significant differences were observed in either case. However, results following a quadratic detrend were nearly identical to results without detrending, and results following filtering had some similarities to ALFF.

Motion parameters

For motion parameters, to ensure even minor motion differences between groups would be detected, a significance threshold of $p \leq 0.50$ was also tested. Whether the threshold for significance was set at 0.05 or 0.50 for SGoF, the results were identical, suggesting Type II errors did not influence motion results.

Discussion

Certain p values deemed nonsignificant when corrected for multiple comparisons were as low as 1.60×10^{-3} (Table 1). Some of these results may be incorrectly non rejected null hypotheses, that is, Type II statistical errors. Therefore, it is worth considering if the conclusions of this study would have been different had these null hypotheses been rejected. The nonsignificant but <0.05 p values for eyes open versus eyes closed included ALFF with nuisance regression performed and short-range FCD with zeros included. The nonsignificant but <0.05 p values for network versus network included FCD and nzFCD. These results being significant would not have changed the conclusions of this study, however, and provide additional support for the observation (Fig. 4E and Table 2) that FCD measures some of the same network to network variation as FALFF. Indeed, network versus network does become statistically significant if a lower r threshold is used which also reduced error (Supplementary Fig. S2). Therefore, if one or more of the results with $8.9 \times 10^{-4} < p \leq 0.05$ were Type II statistical errors, it would not have unduly influenced the conclusions of this study.

Section S7: The Effects of Regression on Potential R-fMRI Biomarkers

Methods

To clarify which regressions caused which effects, four additional types of nuisance signal regression were conducted for short-range FCD analysis: (iii) as the regressions done in the main study, but not regressing the mean signal from the whole-brain mask, (iv) as the regressions done in the main study, but not regressing the mean signals from the whole-brain mask or the CSF mask (thus only white matter and motion parameters), (v) as the regressions done in the main study, but not regressing the mean signals from the whole-brain or white matter masks (thus only CSF and motion parameters), (vi) as ii above, but not regressing the mean signals from the whole-brain, white matter, or CSF masks (thus only motion parameters). All regressions in the main study and Supplementary Data are listed in Supplementary Table S4. (Note that, whether regression of motion parameters was done or not, all data analyzed still included the motion correction as described in Section S1.)

Results

Regression of white matter, CSF, and motion parameters (iii), just white matter and motion parameters (iv) or just CSF and motion parameters (v) produced results similar to performing all regressions (ii). p values were above the significance threshold for the main study for eyes open versus eyes closed ($p = 0.10$, 1.2×10^{-3}, and 0.94, respectively; threshold at $p \leq 8.9 \times 10^{-4}$), far below the significance threshold for network versus network ($p = 2.4 \times 10^{-11}$, 4.3×10^{-11}, and 1.4×10^{-11}, respectively), and nonsignificant for interaction ($p \geq 0.98$ for all three).

Conversely, if only the motion parameters were regressed (vi), results were similar to not performing any regression (i). A p value was produced below the significance threshold for the main study for eyes open versus eyes closed ($p = 2.3 \times 10^{-4}$), above the significance threshold but still less than 0.05 for network versus network ($p = 1.6 \times 10^{-3}$), and not significant for interaction ($p = 1.0$).

Discussion

Thus, using regression of any one of the large-scale, mean, R-fMRI signals (including white matter or CSF) was similar to performing all nuisance regressions (which included the whole-brain signal), whereas regression of just the motion parameters was similar to not performing nuisance regression at all. This is unusual as previous studies have demonstrated differing signal variance and temporal features in white matter versus gray matter (Birn et al., 2008; Chang and Glover, 2009; Chang et al., 2009). As combined PET-MRI scanners are still comparatively new, this similarity is somewhat troubling. Future work should compare these results to results from a stand-alone MRI scanner to determine whether this might be an artifact within the center of the image (where white matter is located) due to the differing hardware setups.

While all forms of FCD and ALFF showed a similar state change as CMR_{glc}, performing the regression step of preprocessing eliminated this (Supplementary Figs. S3 and S4). The regression of signals before calculating broadband variance and FALFF produced results that were very similar to results without the regression step, including statistical significance (Table 1).

There has been controversy regarding whether to regress the global signal (Fox et al., 2009; Murphy et al., 2009). The antiregression argument is correct about the massive changes global regression creates (e.g., Supplementary Fig. S3), whereas the anticorrelated networks it reveals in human brains do not appear to be a mere artifact, for example, giving subjects caffeine produces similar effects to performing regression (Wong et al., 2012). Instead of a general suggestion to regress or not regress, perhaps the decision should be made based on what is being measured. Work by Xu et al. (2014) and Yuan et al. (2014) suggested that measurement of ALFF and FALFF in specific brain

regions may be improved by using regression, whereas this study suggests that measurement of global or metabolic changes (also in ALFF, Table 1) should be done without regression.

Section S8: Numerical Verification of Multimodal Image Registration

Methods

To quantify the quality of registration of the three modalities (BOLD, fluoro-deoxyglucose [FDG], and anatomical MRI) the overlap between the whole-brain masks were calculated. Separate whole-brain masks for each modality were calculated by taking anywhere the sum of the gray matter, white matter, and CSF probability maps (from SPM8) were greater than 0.1. To avoid slices outside the brain (and as the cerebellum was not fully imaged in some subjects) only the 30th through 64th (of 91) slices were taken. The percentage overlap between each pair of modalities was calculated as the number of voxels present in both modalities' masks divided by the number of voxels present in one modality's mask (taking the smaller if the two masks had different numbers of voxels in them).

Results

Overlap was very high in all cases (p values are from two-tailed T tests with equal variance between conditions). Anatomical MRI and BOLD overlap ranged from 97.3% to $\sim$100% and had $p=0.98$. Anatomical MRI and FDG overlap ranged from 98.6% to $\sim$100% and had $p=0.0036$. BOLD and FDG overlap ranged from 97.0% to 99.9% and had $p=0.74$. These results are shown in Supplementary Figure S6.

Discussion

There is a small (0.45%) but significant difference in overlap between the eyes closed and eyes open groups only when comparing anatomical MRI and FDG whole-brain maps. This should not have affected the results of our study as we only compared BOLD and FDG-derived metrics (whose registration did not show a significant difference between conditions).

The significant difference in anatomical MRI/FDG overlap may result may occur due to FDG values being globally higher in the eyes open condition (Figs. 2 and 3), which could hypothetically obscure the underlying anatomy and thus decrease the accuracy of the registration (in particular relative to the registration of the anatomy).

While we did not examine any anatomical metrics here, researchers comparing FDG-PET to anatomical metrics (e.g., voxel-based morphometry or cortical thickness) should take this into account in the future.

Section S9: Effect of Gray Matter Normalization on FDG Data

Methods

Data analysis and processing was identical to the main study, except that before calculating means in networks, the FDG data were divided by the mean value from all voxels from gray matter.

Results

Results are shown in Supplementary Figure S9. For data with gray matter normalization, there was no longer a significant eyes open versus eyes closed difference ($p=0.80$), however, there was a highly significant network versus network difference ($p=2.5\times10^{-132}$). There was a nonsignificant (using the p cutoff from the main study) but much lower p value for interaction between state and network ($p=0.017$).

If individual T-tests are performed for each network's eyes open versus eyes closed states, there are no significant results (using the p cutoff from the main study, $0.012>p>0.97$). However, the p value for only one network is less than 0.05, IC#18 corresponding to the posterior cingulate cortex ($p=0.012$).

Discussion

As the main study focused on a change in mean FDG across the brain differing between states, the gray matter normalization step was not performed because it would have eliminated the ability to measure this result. If gray matter normalization of FDG is performed, it amplifies network versus network differences at the cost of not observing eyes open versus eyes closed differences on a global level.

Individual tests of eyes open versus eyes closed for each network show a nonsignificant but low p value difference between states in the posterior cingulate cortex. Thus, this particular region's state difference between states is still present to a greater degree than other regions. This illustrates how gray matter normalization highlights local differences in FDG.

Section S10: Variance of Motion Parameters

In addition to the maximum deviation used in the main study, the variance of motion parameters was tested as well. For translation the p values were 0.0065 for direction versus direction, 0.13 for eyes open versus eyes closed, and 0.22 for interaction. For rotation the p values were 4.4×10^{-4} for direction versus direction, 0.98 for eyes open versus eyes closed, and 0.91 for interaction. These results are very similar to the reported results for maximum deviation in the main study.

Section S11: Frequency Profile of Detrending

Introduction

The Fourier transformation of a linear or quadratic trend is a complicated function, dominated by a negative exponential ($e^{-\omega}$ for frequency ω) that decays quickly, but is still nonzero at any frequency. Therefore, to determine which frequencies are affected by the quadratic detrend in this study (and compare to a linear detrend which is also commonly used), the actual trends must be examined in the frequency domain.

Methods

The quadratic trend that was removed from the whole-brain signal before correlation with voxels was saved for each subject (see Nuisance signal-based metric: whole-brain correlation Section in the main text), and an equivalent linear trend was also calculated and saved for each subject. The quadratic trend that was removed from each voxel before variance calculation (see Section S6 above) was also saved for all voxels and all subjects, and equivalent linear trends were also calculated

and saved for all voxels and all subjects. The absolute value of the fast Fourier transformation (FFT) was calculated for each trend, and was converted into relative units by dividing by the frequency at 0 Hz (the ''direct current (DC)'' frequency) and multiplying by 100%. Mean and standard deviation was calculated for each group of trends' FFTs at each frequency. Note that, as we are taking the mean of the FFT results of trends that differ for every voxel, the whole-brain signal's trend's FFT will not necessarily be similar to the mean of individual voxels' trends' FFTs.

Results

Results are shown in Supplementary Figure S1. There is little difference between linear and quadratic detrends except at the very lowest frequencies (<0.005 Hz) where the linear trend has slightly greater amplitude, indicating that linear detrend has a slightly greater impact on these frequencies than quadratic detrend. Otherwise, linear and quadratic are very similar. The whole-brain signal's trend decays very quickly as frequency increases, as does the trend for individual voxels, which have had regression performed on them. The decay is much more slow if whole-brain regression was not performed, indicating that detrending has a greater effect if regression is not done. All amplitudes are small, dropping to $\sim$1% of the DC amplitude almost immediately (0.0017 Hz is the lowest frequency shown) and then dropping further to 0.1% of the DC amplitude and decaying quickly.

Discussion

As expected, the frequencies affected by the trends appear visually similar to negative exponentials and, while all frequencies are affected, the greatest effect is at the lowest frequencies. Little difference (in particular in the pass-band of 0.01–0.08 Hz) is visible between quadratic and linear detrends, so it is unlikely our choice here had any effect. Interestingly, the global signal itself, despite being averaged across many voxels, still has a sufficient trend to impact the low frequencies and thus regressing it reduces the effect of any detrend (linear or quadratic) done postfiltering.

References

Birn RM, Smith MA, Jones TB, Bandettini PA. 2008. The respiration response function: the temporal dynamics of fMRI signal fluctuations related to changes in respiration. Neuroimage 40:644–654.

Buckner RL, Sepulcre J, Talukdar T, Krienen FM, Liu H, Hedden T, et al. 2009. Cortical hubs revealed by intrinsic functional connectivity: mapping, assessment of stability, and relation to Alzheimer's disease. J Neurosci 29:1860–1873.

Carvajal-Rodriguez A, de Una-Alvarez J, Rolan-Alvarez E. 2009. A new multitest correction (SGoF) that increases its statistical power when increasing the number of tests. BMC Bioinformatics 10:209.

Chang C, Cunningham JP, Glover GH. 2009. Influence of heart rate on the BOLD signal: the cardiac response function. Neuroimage 44:857–869.

Chang C, Glover GH. 2009. Relationship between respiration, end-tidal CO_2, and BOLD signals in resting-state fMRI. Neuroimage 47:1381–1393.

Chen S, Ross TJ, Zhan W, Myers CS, Chuang KS, Heishman SJ, et al. 2008. Group independent component analysis reveals consistent resting-state networks across multiple sessions. Brain Res 1239:141–151.

Cordes D, Haughton V, Carew JD, Arfanakis K, Maravilla K. 2002. Hierarchical clustering to measure connectivity in fMRI resting-state data. Magn Reson Imaging 20:305–317.

Correa N, Adali T, Calhoun VD. 2007. Performance of blind source separation algorithms for fMRI analysis using a group ICA method. Magn Reson Imaging 25:684–694.

Damoiseaux JS, Rombouts SA, Barkhof F, Scheltens P, Stam CJ, Smith SM, et al. 2006. Consistent resting-state networks across healthy subjects. Proc Natl Acad Sci U S A 103:13848–13853.

Fox MD, Snyder AZ, Vincent JL, Corbetta M, Van Essen DC, Raichle ME. 2005. The human brain is intrinsically organized into dynamic, anticorrelated functional networks. Proc Natl Acad Sci U S A 102:9673–9678.

Fox MD, Zhang DY, Snyder AZ, Raichle ME. 2009. The global signal and observed anticorrelated resting state brain networks. J Neurophysiol 101:3270–3283.

Franco AR, Pritchard A, Calhoun VD, Mayer AR. 2009. Interrater and intermethod reliability of default mode network selection. Hum Brain Mapp 30:2293–2303.

Holmes CJ, Hoge R, Collins L, Woods R, Toga AW, Evans AC. 1998. Enhancement of MR images using registration for signal averaging. J Comput Assist Tomogr 22:324–333.

Majeed W, Magnuson M, Hasenkamp W, Schwarb H, Schumacher EH, Barsalou L, et al. 2011. Spatiotemporal dynamics of low frequency BOLD fluctuations in rats and humans. Neuroimage 54:1140–1150.

Margulies DS, Bottger J, Long X, Lv Y, Kelly C, Schafer A, et al. 2010. Resting developments: a review of fMRI postprocessing methodologies for spontaneous brain activity. MAGMA 23:289–307.

Meindl T, Teipel S, Elmouden R, Mueller S, Koch W, Dietrich O, et al. 2010. Test-retest reproducibility of the default-mode network in healthy individuals. Hum Brain Mapp 31:237–246.

Murphy K, Birn RM, Handwerker DA, Jones TB, Bandettini PA. 2009. The impact of global signal regression on resting state correlations: are anti-correlated networks introduced? Neuroimage 44:893–905.

Tomasi D, Volkow ND. 2010. Functional connectivity density mapping. Proc Natl Acad Sci U S A 107:9885–9890.

Tomasi D, Volkow ND. 2011. Functional connectivity hubs in the human brain. Neuroimage 57:908–917.

van den Heuven MP, Hulshoff Pol HE. 2010. Exploring the brain network: a review on resting-state fMRI functional connectivity. Eur Neuropsychopharmacol 20:519–534.

Wong CW, Olafsson V, Tal O, Liu TT. 2012. Anti-correlated networks, global signal regression, and the effects of caffeine in resting-state functional MRI. Neuroimage 63:356–364.

Xu P, Huang R, Wang J, Van Dam NT, Xie T, Dong Z, et al. 2014. Different topological organization of human brain functional networks with eyes open versus eyes closed. Neuroimage 90:246–255.

Yuan BK, Wang J, Zang YF, Liu DQ. 2014. Amplitude differences in high-frequency fMRI signals between eyes open and eyes closed resting states. Front Hum Neurosci 8:503.

Zou QH, Zhu CZ, Yang Y, Zuo XN, Long XY, Cao QJ, et al. 2008. An improved approach to detection of amplitude of low-frequency fluctuation (ALFF) for resting-state fMRI: fractional ALFF. J Neurosci Methods 172:137–141.

Zuo XN, Kelly C, Adelstein JS, Klein DF, Castellanos FX, Milham MP. 2010. Reliable intrinsic connectivity networks: test-retest evaluation using ICA and dual regression approach. Neuroimage 49:2163–2177.